

THE STUDY OF HEAT CHARACTERISTICS FOR MICRO PIN-FIN HEAT SINKS WITH DIFFERENT STRUCTURES

Nailiang KUANG^{1,2}, Guoran LU^{3,4}, Kui LI^{1,2}, Yanmei KONG³, Jiangbin ZHENG¹, Binbin JIAO^{3,*}

¹ School of Computer Science, Northwestern Polytechnical University, Xi'an, China

² Xi'an Institute of Microelectronics Technology, Xi'an, China

³ Institute of Microelectronics, Chinese Academy of Science, Beijing, China

⁴ University of Chinese Academy of Sciences, Beijing, China

* Corresponding author; E-mail: jiaobinb@ime.ac.cn

Heat flux in electronic devices has increased dramatically with the development of advanced IC technology, facing the demand for effective thermal management technology. Micro pin-fin heat sink (MPFHS) has been demonstrated to be capable of improving the heat transfer capability and suppressing temperature rise effectively. In order to elaborate the discrepancy of heat dissipation of the MPFHS due to the cross-section shapes of pin-fin structures a set of heat sink samples with four different shapes, including the Circle-MPFHS, the Square-MPFHS, the Crisscross-MPFHS and the Octagon-MPFHS, are fabricated with micromachining technology. Then, the thermal characteristics are tested by integrating the heat sinks with a Pt film resistor chip as the heating source, and nucleate boiling phenomenon was observed with a high-speed camera. Results showed that concave corners in pin-fin structures increased the specific surface area, but generated low-velocity vortexes in back flow regions, reducing the heat transfer capability. The heat transfer coefficients of the Octagon-MPFHS, the Crisscross-MPFHS and the Circle-MPFHS was increased by 161.9 %, 152.4% and 85.7 % respectively relative to the Square-MPFHS at the flow rate of 147 kg/m²s. The heat transfer coefficients of the Octagon-MPFHS, the Crisscross-MPFHS, the Circle-MPFHS and the Square-MPFHS was increased by 7.27 %, 11.32 %, 2.56 % and 4.76 % when the mass flow rate was increased from 147 kg/m²·s to 295 kg/m²·s. The nucleate boiling phenomenon in the Crisscross-MPFHS showed periodicity and positive feedback effect, resulting in local dry-out and consequent heat transfer capability deterioration. This study will contribute to the design and modification of MPFHS.

Key words: micro pin-fin heat sink, heat transfer coefficient, nucleate boiling

1. Introduction

As the size of electronic devices shrinks with the development of advanced IC technology, the number of transistors per unit area of the chip increases substantially, resulting in continually rising heat flux inside devices [1]. According to the International Technology Roadmap for Semiconductors,

the average heat flux inside chips may exceed 1000 W/cm^2 , which introduces a great demand for effective thermal management technology [2]. Microchannel heat sink (MCHS) has been demonstrated capable of heat dissipation with 710 W/cm^2 [3]. Secondary microchannels [4]–[6], double-layer microchannels [7]–[10] and bionic fractal microchannels [11]–[14] have been innovatively investigated to improve the heat transfer capability. Other strategies have also been proven to be effective, such as phase change material [15]–[17], nanofluid [18]–[20], and flow boiling cooling [21]–[23].

Compared with conventional parallel MCHS, micro-pin-fin heat sink (MPFHS) naturally features many merits, including breaking the boundary layers, generating secondary flow, and promoting nucleate boiling. Lie et al. [24] compared the heat transfer performance of MPFHS with structures of different sizes and observed that the micro-pin-fin structures could accelerate the speed and frequency of bubble departure. Woodcock et al. [25] proposed a novel piranha MPFHS, which achieved effective heat dissipation with up to 1000 W/cm^2 . Lorenzini et al. [26] experimentally studied that non-uniform distribution of pin-fin structures could slightly improve heat transfer capability via more dense pin-fin structures at the hotspot with a relatively large increase of pressure drop. Heo et al. [27] proved that the viscosity and lower Poiseuille number could be reduced by increasing the surface roughness of pin-fin structures. Chen et al. [28] simulated the effects of surfaces with different hydrophilic and hydrophobic characteristics on the growth, coalesce and removal of bubbles, which showed that the hydrophilic side wall with hydrophobic top favors the growth and removal of bubbles.

However, most of the studies on the thermal characteristics of MPFHS focus on the size and the arrangement of pin-fin structures, or modifying the surface characteristics of the solid structure (such as roughness, hydrophilicity, and hydrophobicity). The dependence of heat transfer capability on geometry parameters has not been characterized clearly with different pin-fin structures, especially fabricated with silicon substrate. In micro-scale forced convection heat dissipation, the change of cross section shape forms different flow and temperature fields, which will affect the generation, coalesce, and escape of bubbles, and ultimately affect the heat transfer capability of the heat sink. Although numbers of inspired pin-fin structures have proposed and demonstrated, it is still unknown which geometric feature plays the decisive role in the enhancement of heat transfer capability. The analysis of geometric detailed features has a guiding significance for the design of new structures in the future.

In this study, MPFHS samples with different cross-sections of a) Circle; b) Square; c) Crisscross; d) Octagon were proposed and fabricated with silicon through MEMS technology. With a Pt resistor chip as the heating source, experiments based on a test module were conducted. The heat transfer capability of heat sinks with different pin-fin structures was comprehensively compared and the flow boiling phenomenon as well as local dry-out was observed. Also, enhancement mechanism behind changing pin-fin structures was explored.

2. Experimental study

2.1 Fabrication

Fig. 1 shows cross-section shapes and geometry parameters of four different pin-fin structures, which have the same characteristic length and height of $60 \mu\text{m}$ and $250 \mu\text{m}$, respectively. All pin-fin structures are fabricated in a staggered arrangement with a pitch width of $100 \mu\text{m}$ on the substrate of

250 μm thick. Deionized water is chosen as the coolant, flowing along the direction as marked by the blue arrows. Fabrication process flow of MPFHS is shown in Fig. 2. After cleaning, thermal oxidation and lithographical patterning, pin-fin structures were etched through DRIE, a typical MEMS dry etching technology, on a 4-inch double-sided polished silicon wafer. To form inlet and outlet, similar process was applied on the other side of the wafer. Through silicon-glass anode bonding, a transparent BF33 glass with the same thickness are bonded on the top of silicon pin-fin structures. Microscope pictures of MPFHS fabricated as above are shown in Fig. 3. Detailed geometry parameters are listed in Table 1.

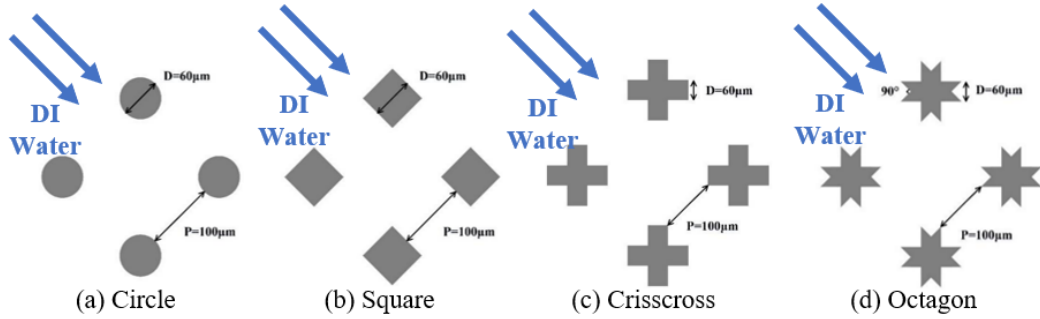


Figure 1. Diagrams of MPFHS with cross-section shapes of (a) Circle; (b) Square; (c) Crisscross; (d) Octagon.

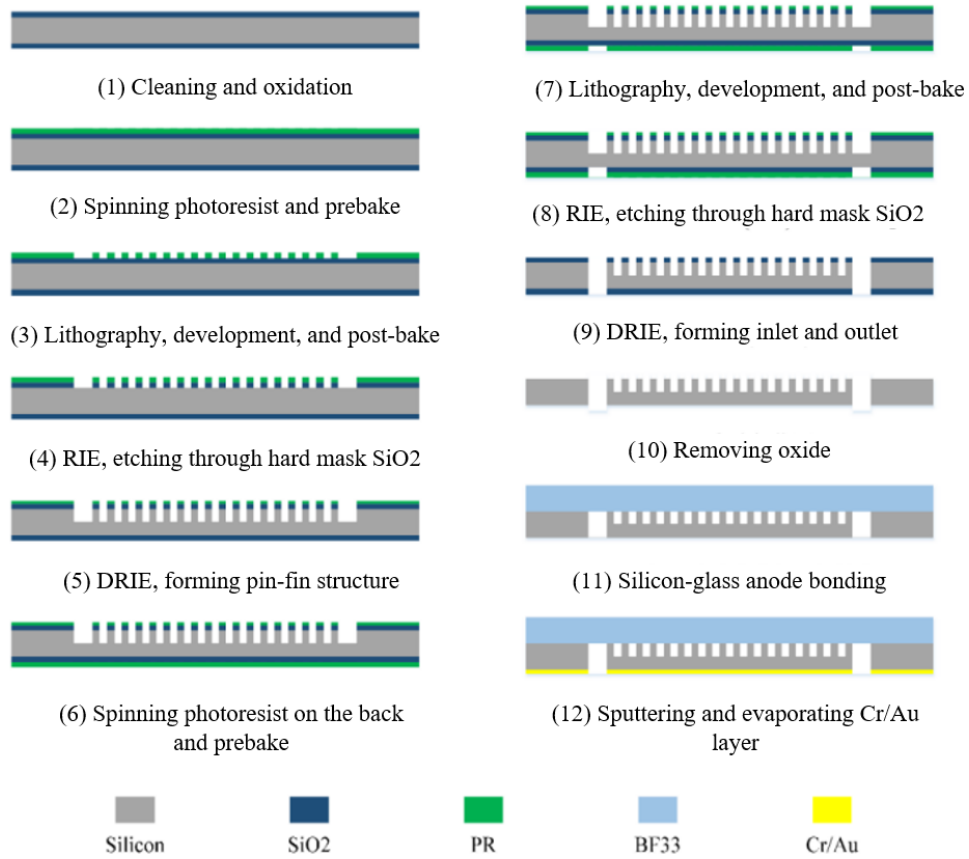


Figure 2. Detailed process flow for MEMS fabrication of MPFHS

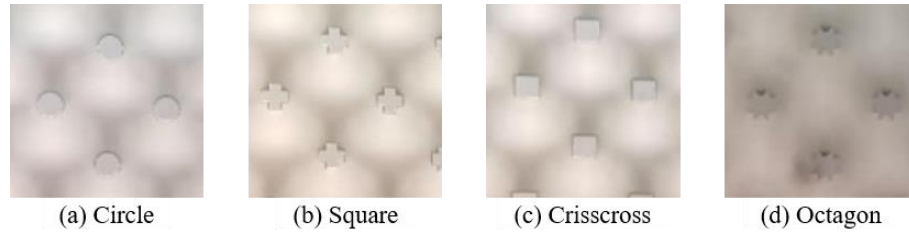


Figure 3. Microscope pictures of MPFHS fabricated by MEMS fabrication technology

Table 1 Geometry parameters of MPFHS with different pin-fin cross section.

Cross-section	Geometry parameters (mm ³)	The height of micro-pin-fins (mm)	The thickness of the substrate (mm)
Circle	0.495×0.495×0.5	0.25	0.25
Square	0.495×0.495×0.5	0.25	0.25
Crisscross	0.778×0.778×0.5	0.25	0.25
Octagon	0.778×0.778×0.5	0.25	0.25

2.2 Experiment setup and test module

Fig. 4(a) shows the schematic diagram of the experiment setup, which is a closed-loop system mainly consisting of a water storage tank, a water pump, the test module, a power supply, a high-speed camera, and a computer for data acquisition. As heating power increases, temperature was sensed by the thermal couples attached on the test module. When coolant temperature reaches the phase transition temperature, the onset of nucleate boiling (ONB) occurs. In order to observe the boiling phenomenon, a high-speed camera was placed directly above the heat sink, capturing images through the transparent BF33 glass. The photos of the whole setup are shown in Fig. 4(b). During experiments, deionized water was stored in a tank to maintain its temperature at 25 °C, and pumped through the heat sink at a constant mass flow rate.

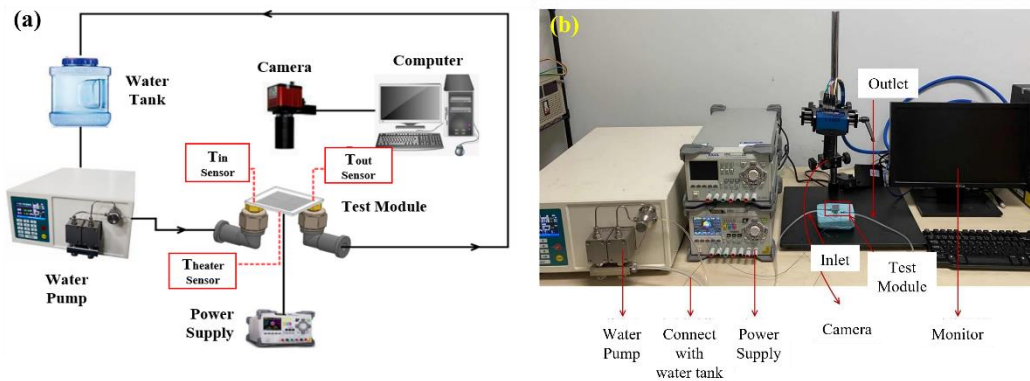


Figure 4. (a) The schematic diagram and (b) photos of experimental setup.

All experiments utilize a chip that consists of Pt resistors as the heating source. Fig. 5(a) shows how the heating chip was installed on the heat sink. Ti (with a thickness of 15 nm) and Pt (with a thickness of 200 nm) were sputtered on a 4-inch silicon wafer successively to form film resistors and the wafer was finally cut into several 3*3 mm² chips. To attach the chip to the heat sink without sacrificing thermal resistance, adhesive made from a mixture of silicon grease and silicone rubber was used, which both reduces the contact thermal resistance and ensures the strength of adhesion. Fig. 5(b) shows the detailed constructure of the test module, which consists of inlet and outlet tube, heat sink and heating chip. Two nuts were weld directly on the inlet and outlet to make connection between the heat sink and two quick connectors. And inlet and outlet tubes were connected to the quick connectors for subsequent experiments.

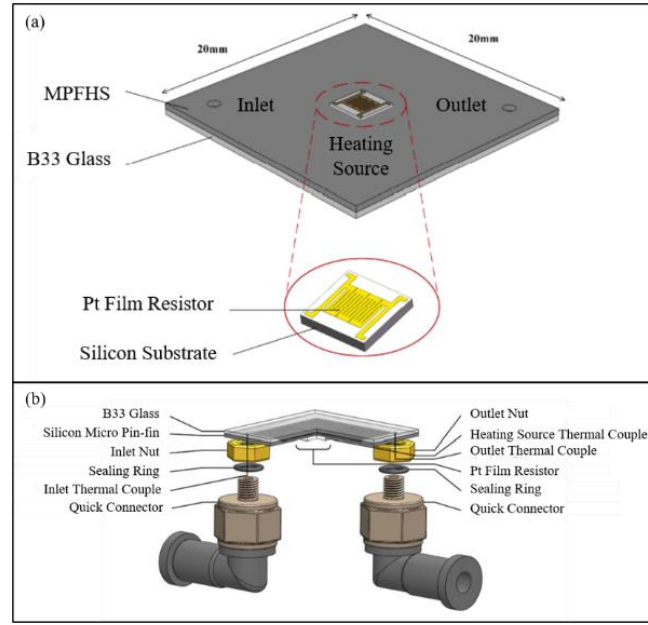


Figure 5. The diagram of (a) mounting of heating chip and (b) the whole test module.

Before attaching the heating chip, the leakage test for the test module was conducted by connecting the inlet and outlet tubes and pumping deionized water through the inlet as shown in Fig. 6(a) and (b). After ensuring no coolant leakage occurring, the heating chip was attached on the heat sink along with its interface PCB. Afterwards, K-type thermocouples were attached to the inlet, outlet, and heating chip surface respectively to record the inlet temperature, T_{in} , outlet temperature, T_{out} and heating chip surface temperature, T_{heater} .

2.3 Temperature Measurement

The chip was directly attached to the heat sink, which makes it difficult to directly measure the temperature of the heat source (the temperature at the interface between the chip and the heat sink) with thermocouples. Therefore, indirect measurement method was adopted. Considering that the heat generated by heaters inside the chip would transfer to the outer surface of the chip and surrounding area of the interface, the average value was taken as the heating chip surface temperature, T_{heater} . As shown in Fig. 6(c), a thermocouple was attached directly on the chip. And another one was attached on the heat sink but coated by the copper wire mesh, reducing the influence of the attachment position on the measured temperature due to the temperature gradient. Finally, the complete test module utilized in

subsequent experiments is shown in Fig. 6(d).

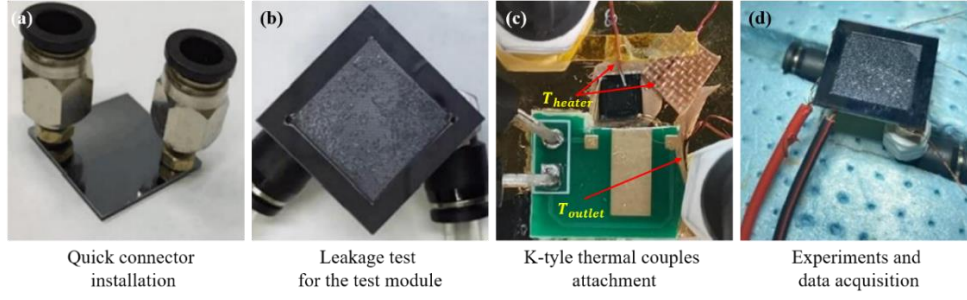


Figure 6. The assembly of the test module.

2.4 Test procedure

Experiments were performed at three mass flow rate ($G = 147, 221, 295 \text{ kg/m}^2\text{s}$). Coolant was pumped through the heat sink without heating for 30 minutes to clear the residual air, after which the heating power was applied and increased in steps. Due to the volume of the tank which is far greater than that of the heat sink, the temperature change brought by the returned outlet coolant is negligible. All measured temperature data are recorded only if the fluctuation is within 2°C for 2 minutes.

2.5 Data reduction

Assuming one-dimensional heat conduction, the total heat flux is generated by the heating chip, which is dominated by Joule's law:

$$q'_{total} = \frac{U^2}{AR} \quad \#(1)$$

where q'_{total} is the total heat flux, U the DC bias voltage, R the resistance of Pt resistor and A the area of the heating chip. Neglecting the heat loss to the ambient, all the heat is transferred and absorbed by the flow:

$$q'_{eff} = q'_{total} = \frac{U^2}{AR} \quad \#(2)$$

where q'_{eff} is the effective heat flux.

Consequently, the heat transfer coefficient h can be calculated using Newton's cooling law:

$$h = \frac{q'_{eff}}{T_{heater} - T_{in}} \quad \#(3)$$

where T_{heater} and T_{in} are the temperature of bottom wall and inlet water measured by K-type thermal couples, respectively.

3. Results and discussion

3.1 Thermal characteristics of different MPFHS

Fig. 7(a)-(c) shows the boiling curves of four different MPFHS samples under three different mass flow rates, where ΔT is defined as $\Delta T = T_{heater} - T_{inlet}$. Under all tested mass flow rates, Crisscross-MPFHS and Octagon-MPFHS had similar boiling curves and achieved obviously higher

heat transfer capability than the other two.

When $G = 221 \text{ kg/m}^2\cdot\text{s}$ and $G = 295 \text{ kg/m}^2\cdot\text{s}$, no ONB occurs. But at a relatively low flow rate of $147 \text{ kg/m}^2\cdot\text{s}$, ONB occurs in Square-MPFHS and Crisscross-MPFHS, at a similar effective heat flux. Although the gap of effective heat flux between two structures is only 11.9 W/cm^2 at ONB, the temperature differences of Crisscross-MPFHS and Square-MPFHS are $40.3 \text{ }^\circ\text{C}$ and $99.3 \text{ }^\circ\text{C}$ respectively. By comparison, it is much easier for Crisscross-MPFHS to transit into two-phase flow. However, the slope of boiling curve at ONB decreases for the Crisscross-MPFHS while that of the Square-MPFHS remain constant relatively, indicating that the heat transfer capability is not enhanced, which will be analyzed in the following section.

Heat transfer coefficient was also calculated and shown in Fig. 8. Heat transfer coefficient was relatively constant as effective heat flux increase before ONB, implying that heat transfer coefficient h has little dependence on the effective heat flux q'_{eff} in the single-phase convection heat transfer. Importantly, no significant enhancement but deterioration of the heat transfer coefficient was observed after ONB for Square-MPFHS, which is consistent with the boiling curve. The list of average values of h in Table 2 shows that, when $G = 147 \text{ kg/m}^2\cdot\text{s}$, h of the Circle-MPFHS, the Octagon-MPFHS and the Crisscross-MPFHS are enhanced by 86 %, 152 % and 162 % respectively, relative to that of the Square-MPFHS. And it is worth noting that Crisscross-MPFHS is least enhanced because of the deteriorated heat transfer capability after ONB.

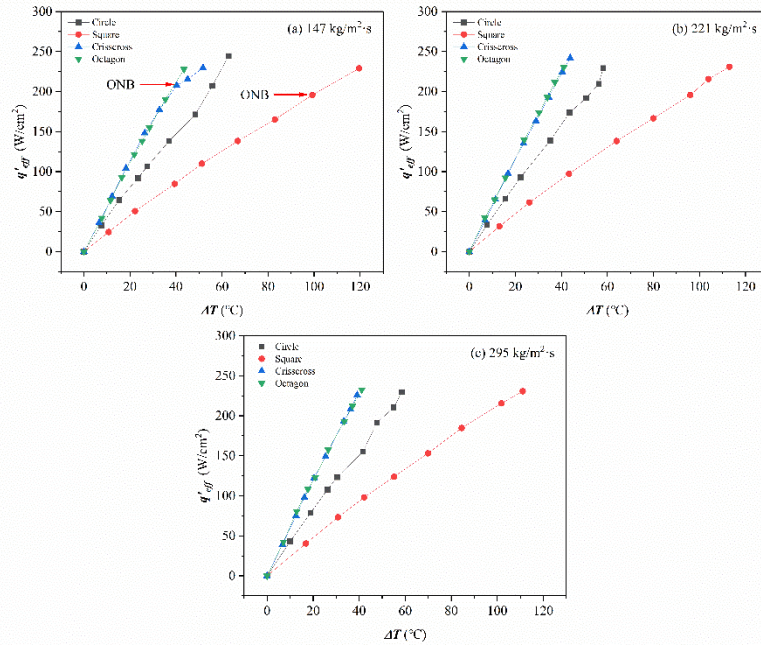


Figure 7. The boiling curves of different heat sinks under different flow rate.

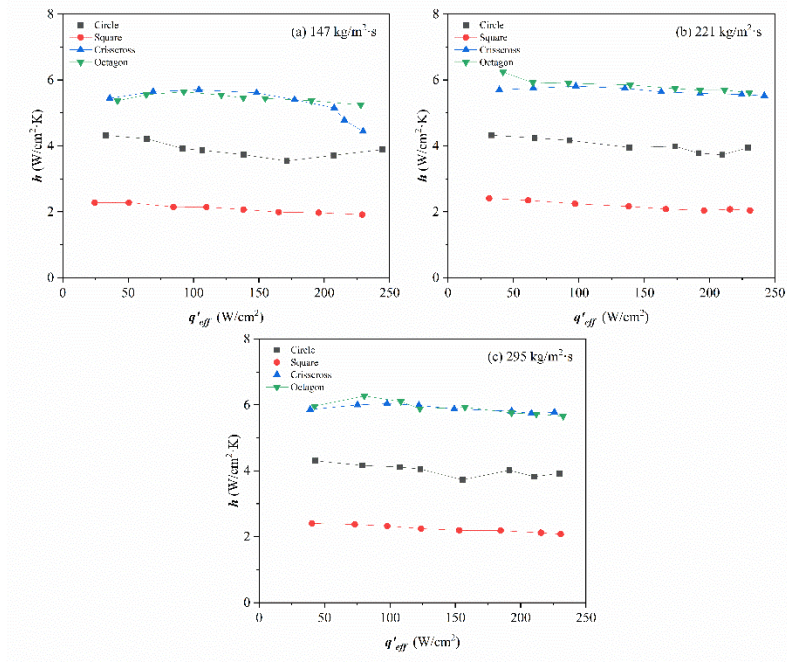


Figure 8. Relationship between heat transfer coefficient and effective heat flux of four heat sinks under three mass flow rates.

Table 2 Average heat transfer coefficient of heat sinks with different cross-section shapes

Cross-section	h_{ave}	h_{ave}	h_{ave}	h_{ave}
	[W/cm²K]	[W/cm²K]	[W/cm²K]	[W/cm²K]
	(147 kg/m²s)	(221 kg/m²s)	(295 kg/m²s)	
Circle	3.9	4.0	4.0	4.0
Square	2.1	2.2	2.2	2.2
Crisscross-shape	5.3	5.7	5.9	5.6
Octagon-shape	5.5	5.8	5.9	5.7

As the cross-section shape develops from circle to a sharp multi-concave structure, the specific surface area of the structure increases accordingly, enhancing the heat transfer capability. However, although the specific surface area of the Octagon-MPFHS is larger than that of the Crisscross-MPFHS, the heat transfer coefficient does not change significantly. At the same time, the specific surface area of the Square-MPFHS is larger than that of the Circle-MPFHS, but the heat transfer coefficient is reduced. The reason for this phenomenon may be attributed to the variation of the flow field. Vortices are generated in the backflow region between the same row of adjacent micro pin-fin structures, and the velocity in this region becomes smaller than that in other regions. As shape of the cross-section develops from a smooth structure to a sharp multi-concave structure, the area occupied by velocity vortices with low velocity increases in the back flow area. Similar flow field degeneration also happens in the concave corners. Thus, the average velocity of the whole fluid decreases. When the decrease of the convective heat transfer caused by the decrease of the flow velocity is greater than the increase brought by the increase of the specific surface area, the overall heat transfer intensity will decrease. Crisscross-MPFHS and Octagon-MPFHS have a better balance between these two relatively

opposite mechanisms.

3.2 Effect of increasing mass flow rate

Fig. 9 and Fig. 10 show the boiling curves and heat transfer coefficient variation for each type of heat sink. The enhancement in heat transfer capability brought by the increase of mass flow rate varies among four MPFHS samples. When the flow rate increased from $147 \text{ kg/m}^2\cdot\text{s}$ to $295 \text{ kg/m}^2\cdot\text{s}$, the average heat transfer coefficient increased 3 %, 5 %, 11 %, 7 % for Circle-MPFHS, Square-MPFHS, Crisscross-MPFHS and Octagon-MPFHS, respectively. Crisscross-MPFHS has the highest sensitivity to the mass flow rate, which is also attributed to its better balance between specific heat transfer area increase and flow field disturbance.

However, according to the data listed in Table 2, two changes of mass flow rate both brought improvement for cooling performance in different amplitude. For all four structures, enhancement brought by increasing the mass flow rate from $221 \text{ kg/m}^2\cdot\text{s}$ to $295 \text{ kg/m}^2\cdot\text{s}$ is less than that brought by increasing from $147 \text{ kg/m}^2\cdot\text{s}$ to $221 \text{ kg/m}^2\cdot\text{s}$. Taking Octagon-MPFHS as example, heat transfer coefficient increased by 5 % for the first change but 2 % for the second, which indicates that the enhancement brought by increasing the mass flow rate will gradually saturate.

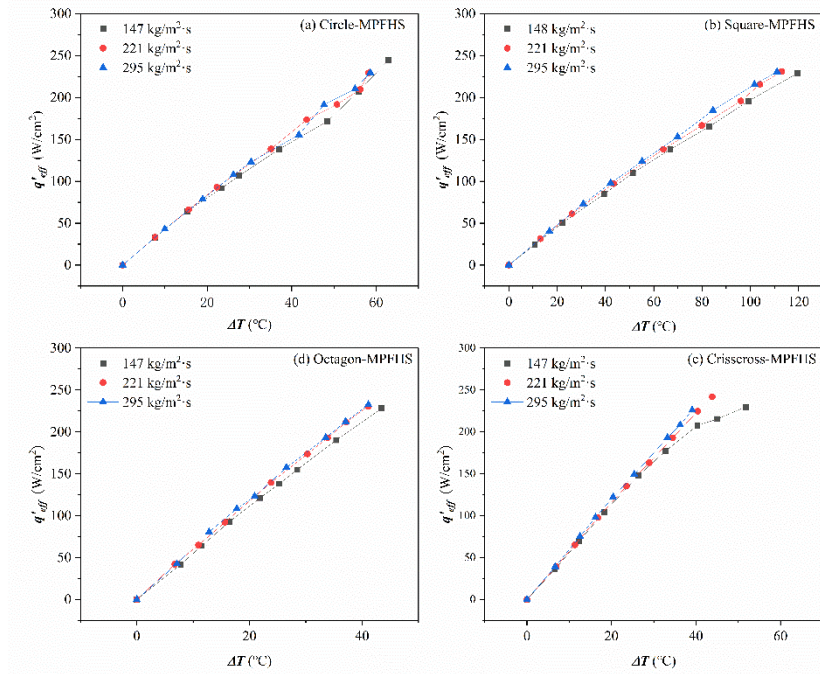


Fig. 9. The change of boiling curves for different heat sinks by increasing mass flow rate.

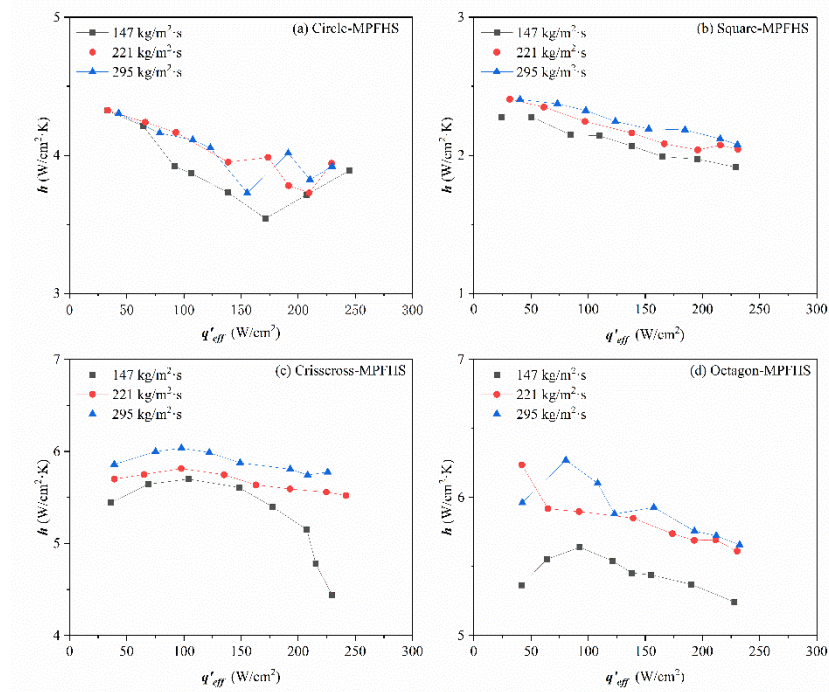


Fig. 10. The change of heat transfer coefficient by increasing mass flow rate.

3.3 Nucleate boiling phenomenon visualization

The high-speed camera focused on the downstream of the Crisscross-MPFHS, where the liquid temperature was relatively higher and the initial boiling occurred. Fig. 11 shows images of the boiling phenomenon at the mass flow rate of 147 kg/m²·s under the heat flux of 207.7 W/cm². When the temperature approached ONB at t_0 , an isolated bubble first appeared at the corner of the pin-fin structure (activated nucleation site). As the temperature increased further, more isolated bubbles appeared, developed, coalesced with adjacent bubbles, and was elongated at $t_0 + 169$ s. Because the viscous force of the coolant on the bubble was greater than that generated by pin-fin structures, the elongated bubble was deformed further along the direction of flow and developed into slug flow. At $t_0 + 323$ s, the deformed bubble reached the outlet, and was flooded out by the flow. It is worth noted that several residual bubbles were generated after the removal of the slug flow.

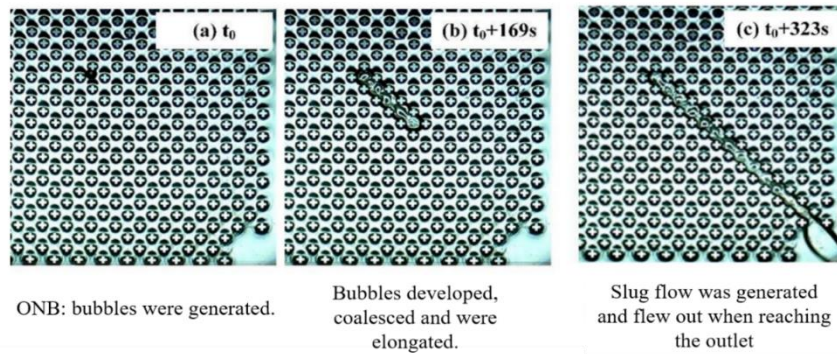


Fig. 11. Process of bubble generation, development, merging, and finally being carried away by the liquid flow.

The heat transfer capability of vapor is relatively lower than that of liquid coolant. Local high temperature appeared near the position where slug flow is formed, activating more nucleation sites. When the fresh liquid rewets the surface, residual bubbles were immediately generated at nucleation sites, initializing the next cycle. As shown in Fig. 12(a) - (d), residual bubbles went through a similar cycle as above, which began at $t_0 + 337$ s. Initially, at $t_0 + 350$ s, isolated residual bubbles were generated at corners of pin-fin structures near the previous elongated bubble, developed and coalesced with each other at $t_0 + 374$ s. At $t_0 + 607$ s, the slug flow appeared, elongated, and was flooded out, after which, as shown in Fig. 12(e), more residual bubbles were generated.

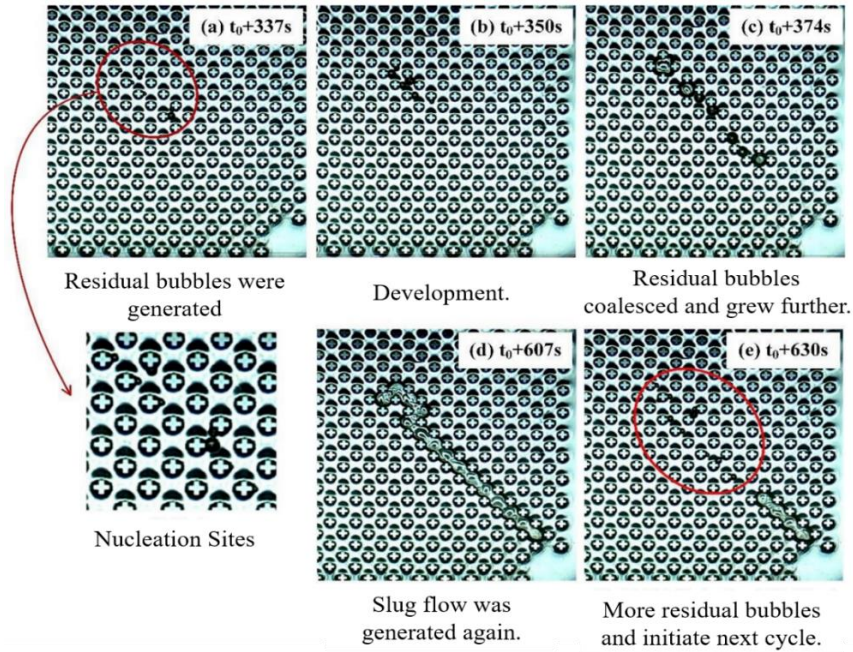


Fig. 12. After slug flow is carried out, more bubbles are generated and entered next cycle.

In the subsequent cycles, the number of residual bubbles and the frequency of the slug flow both increased, resulting in a positive feedback phenomenon. After several cycles, the viscous force brought by the pin-fin structure exceeded that of the flowing liquid on the bubble and bubbles could no longer develop along the flow direction and be flooded out, resulting in local dry-out as shown in Fig. 13. Finally, nucleate boiling transits into film boiling, resulting in local dry-out and dramatical decrease of heat transfer coefficient.

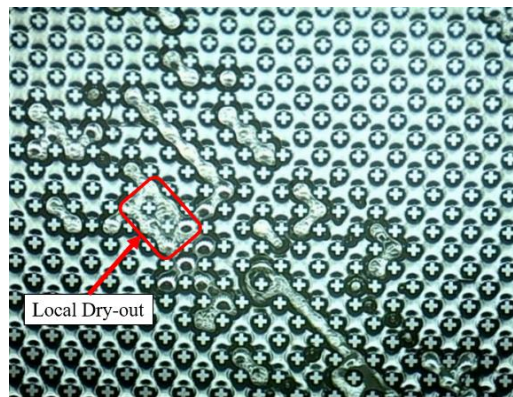


Fig.13. Bubble blockage at the exit of the micro-pillar channel

To avoid the blockage, the heat sink design should guarantee that the viscous force of the flowing liquid on the bubble is always greater than that brought by pin-fin structures. One potential method to reduce the viscous force brought by pin-fin structures is to reduce the number of pin-fin structures attaching to the bubble, which can be achieved increasing the pitch size.

4. Conclusion

In order to study the influence of micro pin-fin structure with different cross-section shapes on the heat transfer capability of MPFHS, based on the fabrication of silicon-based MPFHS, a forced convection heat transfer test platform was established and a series of experiments on the heat transfer capability were performed.

As the cross-section shape develops from circle to a sharp multi-concave structure, the specific surface area of the structure was increased but the velocity of the fluid was reduced. By balancing between two opposite mechanisms, the heat transfer coefficients of the Octagon-MPFHS, the Crisscross-MPFHS and the Circle-MPFHS reached 5.5 W/cm²°C, 5.3 W/cm²°C, 3.9 W/cm²°C respectively at the mass flow rate of 147 kg/m²s, which were enhanced by 162 %, 152 % and 86 % respectively relative to that of the Square-MPFHS.

And the enhancement brought by increasing the flow rate was different among four samples. The heat transfer coefficients of the Octagon-MPFHS, the Crisscross-MPFHS, the Circle-MPFHS and the Square-MPFHS was increased by 7 %, 11 %, 3 % and 5 % when the mass flow rate was increased from 147 kg/m²s to 295 kg/m²s.

The Crisscross-MPFHS was relatively easier to transit into nucleate boiling but the heat transfer capability was reduced after ONB. The deteriorate was not observed in the Square-MPFHS. Through the visualization, nucleate boiling phenomenon in the Crisscross-MPFHS showed periodicity and positive feedback effect. In each cycle, bubbles would go through stages of generation, development, coalesce, elongation and removal. After the slug flow in the previous cycle flowing out, residual bubbles would be generated and initiate the next cycle. After several cycles, local dry-out occurred, resulting in severe blockage inside the heat sink and consequent heat transfer capability degeneration.

By horizontally comparing the thermal characteristics of four MPFHS and visualizing the nucleate boiling, the influence of geometry parameters of the cross-section was comprehensively analyzed. The research in this paper will contribute to the design and modification of MPFHS to improve cooling performance and avoid local dry-out.

Nomenclature

A	contact area of the heating chip, [cm ²]	<i>Acronyms</i>	
G	mass flow rate, [kg/m ² s]	MCHS	microchannel heat sink
h	heat transfer coefficient, [W.cm ² °C]	MPFHS	micro pin-fin heat sink
q'_{eff}	effective heat flux, [W/cm ²]	ONB	onset of nucleate boiling
q'_{total}	total heat flux, [W/cm ²]		
R	resistance, [Ω]		
T_{heater}	temperature of the heater, [°C]		
T_{in}	temperature of the inlet, [°C]		

T_{out} temperature of the outlet, [°C]
 U bias voltage, [V]

References

- [1] C. Bailey, “Thermal Management Technologies for Electronic Packaging: Current Capabilities and Future Challenges for Modelling Tools,” in *2008 10th Electronics Packaging Technology Conference*, Dec. 2008, pp. 527–532. doi: 10.1109/EPTC.2008.4763487.
- [2] C. Nadjahi, H. Louahlia, and S. Lemasson, “A review of thermal management and innovative cooling strategies for data center,” *Sustainable Computing: Informatics and Systems*, vol. 19, pp. 14–28, Sep. 2018, doi: 10.1016/j.suscom.2018.05.002.
- [3] D. B. Tuckerman and R. F. W. Pease, “High-performance heat sinking for VLSI,” *IEEE Electron Device Letters*, vol. 2, no. 5, pp. 126–129, May 1981, doi: 10.1109/EDL.1981.25367.
- [4] A. M. Ali, M. Angelino, and A. Rona, “Numerical analysis on the thermal performance of microchannel heat sinks with Al₂O₃ nanofluid and various fins,” *Applied Thermal Engineering*, vol. 198, p. 117458, Nov. 2021, doi: 10.1016/j.applthermaleng.2021.117458.
- [5] X. Shi, S. Li, Y. Mu, and B. Yin, “Geometry parameters optimization for a microchannel heat sink with secondary flow channel,” *International Communications in Heat and Mass Transfer*, vol. 104, pp. 89–100, May 2019, doi: 10.1016/j.icheatmasstransfer.2019.03.009.
- [6] S. Sabzpooshan and M. Sabouri, “Secondary flow through lateral passages to improve hydrothermal performance of liquid-cooled microchannel heat sinks,” *Applied Thermal Engineering*, p. 120009, Jan. 2023, doi: 10.1016/j.applthermaleng.2023.120009.
- [7] W. He, R. Mashayekhi, D. Toghraie, O. A. Akbari, Z. Li, and I. Tlili, “Hydrothermal performance of nanofluid flow in a sinusoidal double layer microchannel in order to geometric optimization,” *International Communications in Heat and Mass Transfer*, vol. 117, p. 104700, Oct. 2020, doi: 10.1016/j.icheatmasstransfer.2020.104700.
- [8] K. Derakhshanpour, R. Kamali, and M. Eslami, “Improving performance of single and double-layered microchannel heat sinks by cylindrical ribs: A numerical investigation of geometric parameters,” *International Communications in Heat and Mass Transfer*, vol. 126, p. 105440, Jul. 2021, doi: 10.1016/j.icheatmasstransfer.2021.105440.
- [9] A. Maheswari and Y. K. Prajapati, “Thermal performance enhancement and optimization of double-layer microchannel heat sink with intermediate perforated rectangular fins,” *International Journal of Thermal Sciences*, vol. 185, p. 108043, Mar. 2023, doi: 10.1016/j.ijthermalsci.2022.108043.
- [10] H. Shen, H. Liu, X. Shao, G. Xie, and C.-C. Wang, “Thermofluids performances on innovative design with multi-circuit nested loop applicable for double-layer microchannel heat sinks,” *Applied Thermal Engineering*, vol. 219, p. 119699, Jan. 2023, doi: 10.1016/j.applthermaleng.2022.119699.
- [11] C. Ma, Y. Sun, Y. Wu, Q. Zhang, Y. Wang, and G. Ding, “A bio-inspired fractal microchannel heat sink with secondary modified structure and sub-total-sub fluid transmission mode for high heat flux and energy-saving heat dissipation,” *International Journal of Heat and Mass Transfer*, vol. 202, p. 123717, Mar. 2023, doi: 10.1016/j.ijheatmasstransfer.2022.123717.
- [12] H. Li *et al.*, “Effects of inclination angle and heat power on heat transfer behavior of flat heat pipe with bionic grading microchannels,” *Applied Thermal Engineering*, vol. 206, p. 118079, Apr. 2022, doi: 10.1016/j.applthermaleng.2022.118079.

- [13] P. Huang, G. Dong, X. Zhong, and M. Pan, "Numerical investigation of the fluid flow and heat transfer characteristics of tree-shaped microchannel heat sink with variable cross-section," *Chemical Engineering and Processing - Process Intensification*, vol. 147, p. 107769, Jan. 2020, doi: 10.1016/j.cep.2019.107769.
- [14] H. Peng, Y. Du, F. Hu, Z. Tian, and Y. Shen, "Thermal management of high concentrator photovoltaic system using a novel double-layer tree-shaped fractal microchannel heat sink," *Renewable Energy*, vol. 204, pp. 77–93, Mar. 2023, doi: 10.1016/j.renene.2023.01.001.
- [15] R. John Peter, K. R. Balasubramanian, and K. Ravi Kumar, "Comparative study on the thermal performance of microencapsulated phase change material slurry in tortuous geometry microchannel heat sink," *Applied Thermal Engineering*, vol. 218, p. 119328, Jan. 2023, doi: 10.1016/j.applthermaleng.2022.119328.
- [16] B. Rajabi Far, S. K. Mohammadian, S. K. Khanna, and Y. Zhang, "Effects of pin tip-clearance on the performance of an enhanced microchannel heat sink with oblique fins and phase change material slurry," *International Journal of Heat and Mass Transfer*, vol. 83, pp. 136–145, Apr. 2015, doi: 10.1016/j.ijheatmasstransfer.2014.11.082.
- [17] M. Chen, Y. Wang, and Z. Liu, "Experimental study on micro-encapsulated phase change material slurry flowing in straight and wavy microchannels," *Applied Thermal Engineering*, vol. 190, p. 116841, May 2021, doi: 10.1016/j.applthermaleng.2021.116841.
- [18] A. Shahsavari, P. Jha, and I. Baniasad Askari, "Experimental study of a nanofluid-based photovoltaic/thermal collector equipped with a grooved helical microchannel heat sink," *Applied Thermal Engineering*, vol. 217, p. 119281, Nov. 2022, doi: 10.1016/j.applthermaleng.2022.119281.
- [19] S. Rostami, A. A. Nadooshan, A. Raisi, and M. Bayareh, "Numerical assessment of the multi-phase nanofluid flow inside a microchannel during the melting and solidification of PCM in the thermal management of a heatsink," *Engineering Analysis with Boundary Elements*, vol. 148, pp. 267–278, Mar. 2023, doi: 10.1016/j.enganabound.2022.12.038.
- [20] Y. Huang, C. Zou, M. Chen, and H. Sun, "Thermophysical property evaluation of β -cyclodextrin modified ZrO₂ nanofluids for microchannel heat exchange," *Ceramics International*, vol. 48, no. 21, pp. 31728–31737, Nov. 2022, doi: 10.1016/j.ceramint.2022.07.096.
- [21] W. Li, C. Li, Z. Wang, and Y. Chen, "Enhanced flow boiling in microchannels integrated with supercapillary pinfin fences," *International Journal of Heat and Mass Transfer*, vol. 183, p. 122185, Feb. 2022, doi: 10.1016/j.ijheatmasstransfer.2021.122185.
- [22] Y. Lin, Y. Luo, W. Li, and W. J. Minkowycz, "Enhancement of flow boiling heat transfer in microchannel using micro-fin and micro-cavity surfaces," *International Journal of Heat and Mass Transfer*, vol. 179, p. 121739, Nov. 2021, doi: 10.1016/j.ijheatmasstransfer.2021.121739.
- [23] Y. Li and H. Wu, "Experiment investigation on flow boiling heat transfer in a bidirectional counter-flow microchannel heat sink," *International Journal of Heat and Mass Transfer*, vol. 187, p. 122500, May 2022, doi: 10.1016/j.ijheatmasstransfer.2021.122500.
- [24] Y. M. Lie, J. H. Ke, W. R. Chang, T. C. Cheng, and T. F. Lin, "Saturated flow boiling heat transfer and associated bubble characteristics of FC-72 on a heated micro-pin-finned silicon chip," *International Journal of Heat and Mass Transfer*, vol. 50, no. 19–20, pp. 3862–3876, 2007, doi: 10.1016/j.ijheatmasstransfer.2007.02.010.
- [25] C. Woodcock, C. Ng'oma, M. Sweet, Y. Wang, Y. Peles, and J. Plawsky, "Ultra-high heat flux dissipation with Piranha Pin Fins," *International Journal of Heat and Mass Transfer*, vol. 128, pp.

504–515, Jan. 2019, doi: 10.1016/j.ijheatmasstransfer.2018.09.030.

[26] D. Lorenzini *et al.*, “Embedded single phase microfluidic thermal management for non-uniform heating and hotspots using microgaps with variable pin fin clustering,” *International Journal of Heat and Mass Transfer*, vol. 103, pp. 1359–1370, Dec. 2016, doi: 10.1016/j.ijheatmasstransfer.2016.08.040.

[27] K. Y. Heo, K. D. Kihm, and J. S. Lee, “Fabrication and experiment of micro-pin-finned microchannels to study surface roughness effects on convective heat transfer,” *J. Micromech. Microeng.*, vol. 24, no. 12, p. 125025, Dec. 2014, doi: 10.1088/0960-1317/24/12/125025.

[28] B. Chen, Z. Zhou, J. Shi, S. R. Schafer, and C.-L. (C. L.) Chen, “Flooded Two-Phase Flow Dynamics and Heat Transfer With Engineered Wettability on Microstructured Surfaces,” *Journal of Heat Transfer*, vol. 137, no. 9, p. 091021, Sep. 2015, doi: 10.1115/1.4030237.

Submitted: 11.03.2023

Revised: 04.07.2023

Accepted: 12.07.2023